

Anomalous strain rate sensitivity of a Cu/Al₂O₃ multi-layered thin film

Szilvia Kalácska^{a,b,*}, László Pethő^b, Guillaume Kermouche^a, Johann Michler^b, Péter Dusán Ispánovity^c

^aMines Saint-Etienne, Univ Lyon, CNRS, UMR 5307 LGF, Centre SMS, 158 cours Fauriel 42023 Saint-Étienne, France

^bEmpa, Swiss Federal Laboratories for Materials Science and Technology, Laboratory of Mechanics of Materials and Nanostructures, CH-3602 Thun, Feuerwerkerstrasse 39. Switzerland

^cELTE Eötvös Loránd University, Department of Materials Physics, Pázmány Péter sétány 1/a, 1117 Budapest, Hungary

Abstract

To study the size and strain rate dependency of copper polycrystalline microstructures, a multi-layered copper/Al₂O₃ thin film was deposited on a Si substrate using a hybrid deposition system (combining physical vapour and atomic layer deposition). High temperature treatment was applied on the “As Deposited” material with ultrafine-grained structure to increase the average grain size, resulting in a “Heat Treated” state with microcrystalline structure. Focused ion beam milling was employed to create square shaped micropillars with two different sizes, that were subjected to compressive loading at various (0.001/s – 1000/s) strain rates. The detected two distinct anomalies in the strain rate sensitivity behavior appearing at high strain rates could be related to the pillar diameter and the grain size of the deformed samples. The Al₂O₃ interlayer studied by transmission electron microscopy showed excellent thermal stability and grain boundary pinning by precipitation, also resulting in the homogeneous deformation of the pillars and preventing shear localization. Geometrically necessary dislocation densities estimated by high (angular) resolution electron backscatter diffraction presented inhomogeneous dislocation distribution within the deformed pillar volumes, that is attributed to the proximity of the sample edges. Finally, the Al₂O₃ interlayers successfully suppressed any possible recrystallization processes, contributing to the excellent film stability, that makes the proposed coating ideal to be operating under extreme conditions.

Keywords: thin films, micromechanical testing, microstructure, high strain rate, plastic deformation, size effect

1. Introduction

Thin films are employed by a large variety of applications. Protective coatings can improve corrosion or scratch resistance, they can hold decorative purposes (to change the color/roughness of the surface), or they can have other functional objectives. Creating multi-layered thin films with alternating dissimilar sublayers promises unusual (electrical [1], thermal [2], optical [3], etc.) properties to be experimentally investigated. Such systems, where grain size and texture can be controlled by the deposition / annealing process, represent an outstanding opportunity to focus on a few key aspects of the deformation processes driven by the collective behavior of dislocations.

Copper coating is important in several applications due to its excellent conductivity, corrosion resistance [4], and antimicrobial properties. Copper is the most widespread choice as a conducting material for connections in integrated circuits with submicron features [5]. The microstructure of the coating not only influences the thermal and electrical conductivity [6], but also its mechanical properties, too. Therefore, it is important to study the

deposited coating from the structural engineering point of view too.

Hybrid thin film coatings emerged due to their enhanced mechanical properties, such as in Al/Al₂O₃ depositions [7, 8]. Here, the combination of physical vapor deposition (PVD) is combined with atomic layer deposition (ALD). PVD is employed to grow high purity thick layers in a low oxygen environment, while ALD is used to obtain precise thickness control over thinner (typically in the nm range) layers.

Investigating the mechanical stability under various extreme conditions is crucial for defining the margins of the coatings’ applicability. Recent innovations in experimental micromechanical testing now enables probing at a wide range of deformation speeds [9, 10, 11, 12, 13] at the relevant (application) scale. The two essential parameters for understanding deformation kinetics are the strain rate sensitivity (SRS, m) of the flow stress and the activation volume (Ω) [14]. Analyzing these two parameters can provide a clearer understanding of the rate-controlling deformation mechanisms. However, there is limited experimental information on the high strain rate (HSR) regime mechanical behavior as a function of size [15, 16] and microstructure in the literature [17, 18].

The aim of this study is, therefore, to design a hy-

*Corresponding author

Email address: szilvia.kalacska@cnrs.fr (Szilvia Kalácska)

brid (Cu/Al₂O₃) thin film and tailor its microstructure by heat treatment to become a model material in order to study the SRS behavior as a function of sample size and microstructure. The purpose of the Al₂O₃ interlayer was to limit grain growth between the subsequent Cu depositions, allowing to investigate the “As Deposited” (ultrafine-grained) coating parallel to its “Heat Treated” counterpart containing microcrystalline grains.

2. Materials & Methods

2.1. Sample preparation

For the creation of the desired multilayers, a hybrid thin film deposition system combining both ALD and PVD methods was applied (Swiss Cluster). The sequential deposition consisted of alternating (5 times) $\sim 1 \mu\text{m}$ thick pure Cu separated by 10 nm thin Al₂O₃ interlayers deposited on a Si (100) substrate (Fig. 1a) at room temperature. Cross-sectional electron backscatter diffraction (EBSD) confirmed the average grain size of this “As Deposited - AD” film to be $d^{AD} \sim 120 \text{ nm}$ (area weighted mean, see in Fig. 1c,e), qualifying this coating as ultrafine-grained (UFG).

Heat treatment was performed in a furnace at 800°C for 4 hours in Ar gas to evade oxidation, that resulted in the “Heat Treated - HT” sample. The roughness of the film surface along with the average grain size ($d^{HT} \sim 1.1 \mu\text{m}$) has increased considerably, as it can be seen in Fig. 1d,f. The increased grain size defines this coating having microcrystalline (MC) structure.

In order to investigate the cross-section of the coating a sharp edge was prepared by broad beam Ar ion polishing

(Jeol IB-1953CP) with beams of 6 kV (60 mins) and 2 kV (60 mins). For the micromechanical experiments square based taper-free micro-samples were created close to the sharp edge by focused ion beam (FIB) using a FEI Helios 600i and a Tescan Lyra3 Ga⁺ scanning electron microscope (SEM) system (Fig. 1b). Sequential preparatory beams of 30 kV 21 nA (rough milling for removing large amount of material around the region of interest) down to 2.5 – 0.4 nA polishing were utilized with a 45° incident angle direction with respect to the prepared surfaces. Two batch of different sized cuboid pillars ($\sim 4.2 \mu\text{m}$ and $\sim 2.9 \mu\text{m}$ side length) were fabricated to study possible size related effects in the SRS.

2.2. Micromechanical testing

Micro-samples were deformed using an Alemnis ASA nanodeformation system equipped with three different load cells (strain gage based standard and mini load cells for quasi-static strain rates (SR), piezo-based SmarTip for high SRs). For pillar compressions, conductive diamond flat punches (Synton AG) with diameters of 5 μm and 10 μm were utilized. The recorded load-displacement curves were baseline (drift) and compliance corrected using the AMMDA evaluation software. During HSR testing, due to the high acceleration following the tip actuation (achieving up to 6 mm/s tip velocity), an oscillating noise appeared, superimposed to the signal (“ringing effect”). In order to determine the yield stresses σ_y in such difficult cases, the elastic and plastic parts of the stress-strain curves were fitted using a linear equation, and their intersection was used to obtain the apparent yield stress (see Fig. 2a,b and Suppl. Fig. S4 for the full process). This method enabled

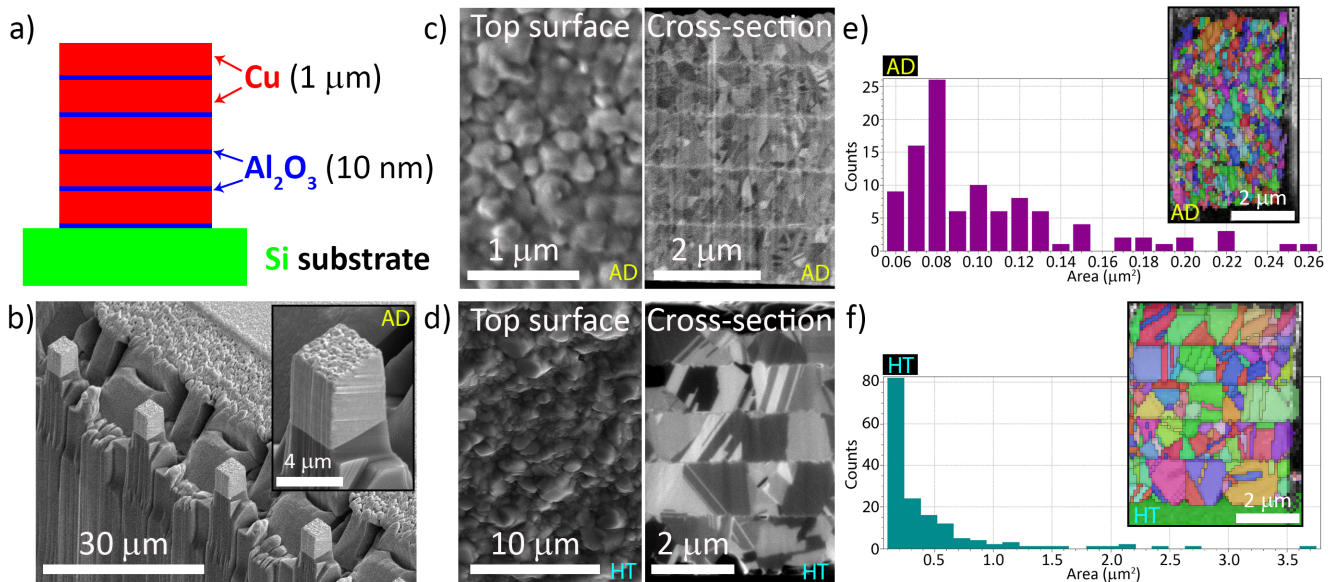


Figure 1: **a)** Schematics of the deposited multi-layered thin film coating, indicating 5 layers of Cu (PVD), separated by thin Al₂O₃ (ALD) layers. **b)** Overview of the FIB-milled batch of the “As Deposited - AD” micropillars. The inset shows one pillar with higher magnification, where the brighter volume corresponds to the deposited thin film. **c)** Top surface and cross-sectional images of the AD coating. **d)** Top surface and cross-sectional images of the “Heat Treated - HT” coating. **e)** Grain size distribution of the AD sample, based on cross-sectional EBSD measurements (inset). **f)** Grain size distribution of the HT sample, based on cross-sectional EBSD measurements (inset).

to avoid further data filtering or averaging in the σ_y determination. For the consistency of the yield stress values at low and high strain rates, all mechanical data were treated the same way.

2.3. Microstructure characterization

EBSD was employed to get statistical information on the grains of the samples. A Zeiss Supra 55 VP FEG-SEM equipped with an Oxford Instruments Symmetry 2 detector was used to record the EBSD diffraction patterns (2x2 binning, frame averaging: 4, step: 80-100 nm). High (angular) resolution (HR-) EBSD was utilized for the geometrically necessary dislocation (GND) density estimation prior to and following the deformation. This technique is based on image cross-correlation, linking each point on the map to a reference stress state [19]. The stored patterns were evaluated using the BLG Vantage CrossCourt Rapide v4.6 HR-EBSD software. *Post mortem* FIB-assisted 3D tomography [20] was performed on two pillars (HT big pillars, deformed at 0.01/s and 1000/s) to study the effect of SR on the microstructure close to the surface and inside the deformed volume.

Transmission electron microscopy (TEM) was used to gain information on the stability of the hybrid layers after high temperature processing. As a result of the heat treatment, the grains were expected to grow, that can disturb the continuity of the deposited thin (10 nm) oxide layer. For this, a Jeol-ARM200F Cold FEG NeoARM Cs-corrected TEM was utilized at 200 kV. This instrument is equipped with an energy dispersive spectroscopy (EDS) detector (SDD CENTURIO-X) too. Mul-

tipple TEM-lamellae were prepared by FIB milling, following the standard preparation recipe, using sequential settings from 30 kV, 21 nA–40 pA (rough milling and liftout) down to 5 kV–1 kV, 20 pA (thinning and final cleaning).

3. Results

The engineering stress (σ_{eng}) - engineering strain (ϵ_{eng}) curves resulting from several pillar compressions at various strain rates ($0.001/s \leq \dot{\epsilon} \leq 1000/s$) are shown in Fig. 2. It is expected that the AD pillars exhibit higher yielding than the HT specimen, according to grain boundary strengthening. This phenomenon is confirmed in Fig. 2a,b for the two types of coatings (AD and HT). Work hardening seems not to be affected by the SR change. It is important to note that in the HT samples, due to the increased coating roughness, the uneven surface can introduce an artefact to the mechanical data. As it can be observed in Fig. 2b (P02, $\dot{\epsilon} = 0.01/s$), if the surface of the pillar contains a part exceeding the average height, upon contact with the flat punch, this grain will start to deform, resulting in a less steep elastic loading (due to the fact that the $\sigma_{eng} - \epsilon_{eng}$ curves are calculated with the full pillar dimensions). However, once the surface is levelled by the indenter tip, the elastic loading part is recovered while the full pillar cross-section is being compressed beyond this point. The primarily deformed grain might locally modify the deformation state of the neighboring grains, however, due to the multilayered nature of the thin film, we expect to see negligible influence of this effect in the global mechanical behavior. To avoid this, either *i*) additional FIB

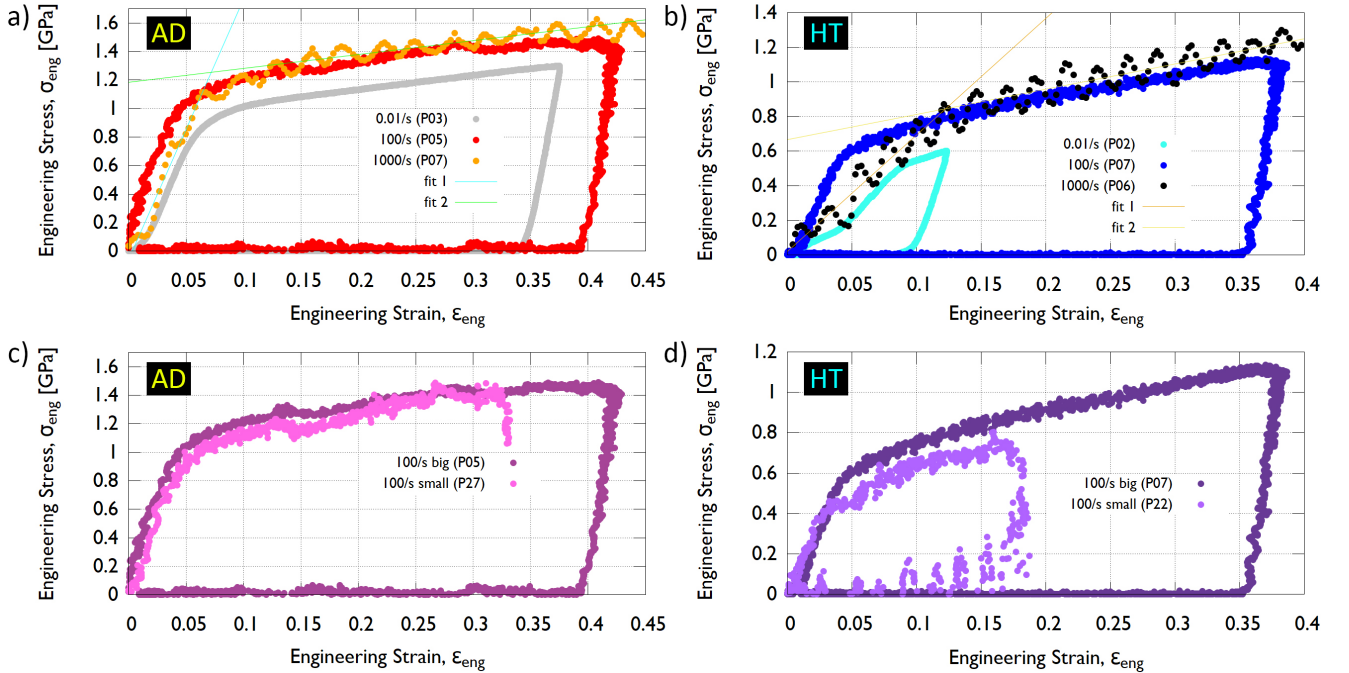


Figure 2: $\sigma_{eng} - \epsilon_{eng}$ curves at various strain rates. a) AD pillars, shown with the linear fits for 1000/s curve (pillar P07) for the yield stress determination. b) HT pillars, shown with the linear fits for 1000/s curve (pillar P06) for the yield stress determination. c) AD pillars with two different sizes at SR=100/s. d) HT pillars with two different sizes at SR=100/s.

polishing could be applied that levels the pillar surface, or *ii*) a Pt deposition cap may be added. Both solution could potentially modify the recorded mechanical data [8], so in this work, we avoid using any of the aforementioned corrections, and restrict ourselves to the analysis of the unmodified HT coating.

Smaller pillars exhibit lower yielding, that can be attributed to the *i*) surface damage caused by FIB milling [21, 22] or *ii*) it can be a grain size effect enhancing strain localization in the smaller HT specimen. As it was mentioned previously, to evade tapering, a higher incident angle of the bombarding ions were utilized, that may result in a higher concentration of implanted Ga close to the pillar surfaces. In smaller pillars, the effect of Ga presence is enhanced due to the increased surface-to-volume ratio. This explanation is the most probable cause of the slight yield stress decrease in smaller pillars rather than other microstructure related effects, since it is apparent in both the AD (UFG) and HT (MC) pillars in a similar manner at both low and high strain rates (see in Fig. 3).

In order to determine the SRS-factor (m), the following equation is used:

$$m = \frac{\partial(\ln \sigma_y)}{\partial(\ln \dot{\epsilon})}. \quad (1)$$

In Fig. 3a, the determined average σ_y values are plotted on a linear scale as a function of $\dot{\epsilon}$ on a logarithmic scale. The error bars show the spreading of the calculated values from repeated pillar compression tests (typically three), that presents good repeatability of the experiments at almost all applied strain rates. As a result of the employed linear fitting method, σ_y can be determined fairly consistently. The shaded area represents the noise during loading, indicating that when a load cell is switched from strain gage based ($\dot{\epsilon} \leq 1/s$) to piezoelectric based detection ($\dot{\epsilon} \geq 10/s$), the noise increases significantly. The drawback of using a noisier (but much stiffer) load cell [10] is compensated by the ability to go beyond the previously achievable deformation speeds and sampling rates.

The noise becomes extremely large then the load signal starts to have a overwhelming oscillation due to the ringing effect ($\dot{\epsilon} = 1000/s$). To reduce this outcome originating from the immense acceleration during the operation (6 mm/s), certain pillars were compressed in a way that the tip acceleration was initiated far ($\sim 14 \mu\text{m}$) away from the surface, anticipating that at this distance the tip resonance decreases to minimal upon impact, when the flat punch is already travelling at its maximum speed [23]. To further improve the mechanical data, some pillars were compressed to very high strains to allow the tip to drive through these pillars at a constant speed without stopping, thereby completely destroying the samples and preventing them from being examined by *post mortem* EBSD analysis (hence the notation “pancake” in Suppl. Fig. S5-S7).

Strain rate sensitivity is plotted in Fig. 3b for all the tested pillars. The fitted dotted lines are used to determine the m values, calculated using Eq. 1. At lower strain rates, the HT samples are expected to behave similarly as the AD samples based on the work of Ramachandramoorthy and Kalacska *et al.* (for more details see the *Discussion* section.) [18], therefore, only one additional $\dot{\epsilon}$ state was tested in this regime. Increased repeatability error in the HT samples are attributed to the surface roughness increase, as stated previously.

In order to understand the effect of heat treatment on the Cu/Al₂O₃ multi-system, TEM-lamellae were prepared from the HT sample via FIB milling. The results shown in Fig. 4 confirm the enlarged grains due to high temperature ageing. Precipitates along grain boundaries were observed with sizes varying between 2-5 nm (Fig. 4c). EDS line profile collected through a Cu/Al₂O₃/Cu interface confirmed the integrity of the Al₂O₃ deposition after heat treatment, and the estimated layer thickness was calculated to be ~ 13.5 nm (Fig. 4d). It is mentioned that this result may depend on the thickness of the lamella.

Finally, the effect of SR on the evolved dislocation structure was investigated by cross-sectional HR-EBSD. The pillars’ surfaces were mapped before and after defor-

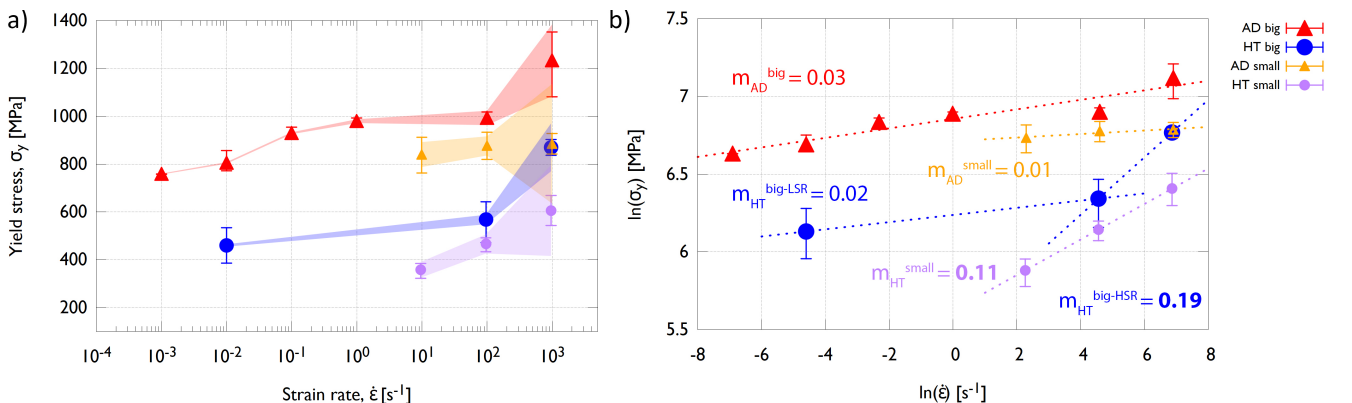


Figure 3: **Strain rate sensitivity of the tested pillars.** **a)** Strain rate (log. scale) – yield stress (linear scale), and **b)** the corresponding logarithmic representation for the SRS-factor (m) determination (based on Eq.1). Error bars are an indication of the spreading of the calculated yield stresses from repeatability tests. The shaded area shows the amount of noise at each strain rate step, while the m values are determined by the fitted dotted lines.

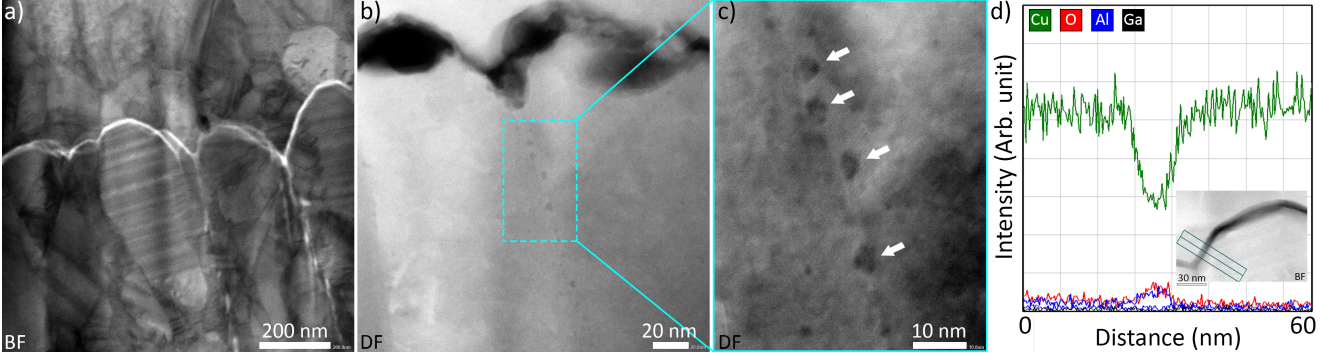


Figure 4: **TEM results.** **a)** Bright field (BF) image of a lamella lifted out from the HT sample, showing the Cu grain structure, together with the Al_2O_3 interlayer (white contrast). **b)** Dark field (DF) image of an area between two larger grains, here the Al_2O_3 layer appears to be black. **c)** Enlarged section of the image in **b)**, showing inter-granular Al_2O_3 precipitates (white arrows). **d)** Chemical composition analysis by EDS performed on the area in the inset measures the Al_2O_3 layer to be ~ 13.5 nm thick.

mation, and the resulting GND density maps are plotted in Fig. 5. Here, the small grains (containing less than 20 pixels) were excluded from the analysis (green areas). Also, patterns with lower band contrast (BC) value than a given threshold ($\text{BC} < 100$) were also removed from the evaluation (i.e. where patterns overlap close to grain boundaries). Afterwards, each identified grain was assigned to a reference pattern, chosen from the same grain with the lowest kernel average misorientation value (black dots). GND densities (ρ_{GND}) were then estimated based on 20 regions of interest for three pillars (P02 – P04).

4. Discussion

Initially, the FIB-milled pillars were chosen to be square shaped for two main reasons: *i)* to allow the monitoring of the ρ_{GND} evolution by HR-EBSD mapping, and *ii)* to create perfect uniaxial loading conditions and identical cross-sections along the height of the pillars for more accurate mechanical data analysis. Looking at the already deformed samples (Suppl. Fig. S2) it can be concluded that the pillars deform in a “barrelling” manner, achieving the largest shape change closer to the top of the specimens at the low strain rate (LSR) regime (softer top). When a pillar is compressed at HSR ($\leq 100/\text{s}$), the shape of the pillars become slightly different, as here the middle of the coating extrudes the most.

Slip plane localization is successfully suppressed by the consecutive Al_2O_3 layers in both the AD and HT samples, hence the resulting smooth $\sigma_{\text{eng}} - \varepsilon_{\text{eng}}$ curves in Fig. 2, that show the absence of large strain bursts (or stress drops). The surface analysis of the deformed pillars support these findings in Suppl. Figs. S2 and S3. Flow stresses reach quite high average values ($\overline{\sigma}_{\text{y}}^{\text{AD}} = 758$ MPa and $\overline{\sigma}_{\text{y}}^{\text{HT}} = 460$ MPa) during quasi-static deformation, much higher than pure Cu in literature, approaching the regime of nanocrystalline copper [24, 25]. This increased yielding could be partly attributed to the grain boundary (Hall-Petch) strengthening (using the already established \bar{d} values for the AD and HT samples with the equation

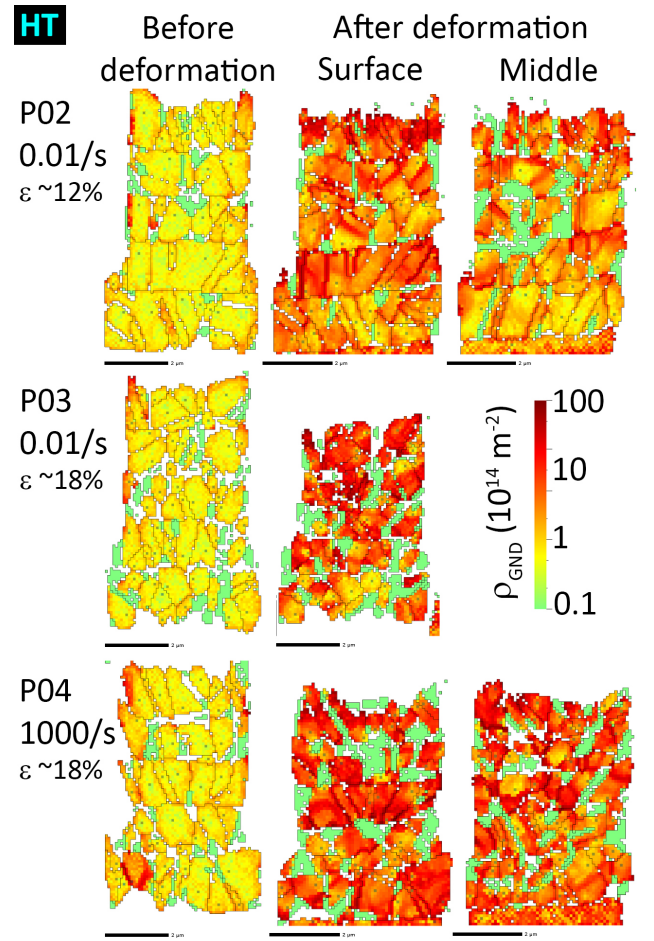


Figure 5: **HR-EBSD results.** Maps were measured on the surface before and after deformation (ε). Pillars P02 and P04 were subjected to serial cross-sectioning by FIB, where the middle of the pillars (about $1.6 \mu\text{m}$ away from the first slice) were also imaged. Black scale bars corresponds to $2 \mu\text{m}$.

$\sigma_{\text{GB}} = \sigma_0 + kd^{-0.5}$ with $\sigma_0^{\text{Cu}} = 25$ MPa material constant and $k = 0.12$ MPa $\text{m}^{1/2}$ strengthening coefficient [26], resulting in $\sigma_{\text{GB}}^{\text{AD}} = 371$ MPa and $\sigma_{\text{GB}}^{\text{HT}} = 139$ MPa theoretical values). Further strengthening mechanisms also play

a key role in raising the σ_y values, such as dislocation and potentially (based on Fig. 4c) precipitation strengthening. As suggested by Fig. 4a, nanotwinning also occurs in this thin film system [27] that could be significant in the HSR behavior in case of possible dynamic recrystallization [28]. Additionally, high angle grain boundaries in the AD sample tend to run along the deformation axis of the pillars (somewhat columnar grain growth resulting in ellipsoid grain shapes), that will also increase the material's resistance towards compressive/tensile stresses.

When we compare the yield stress values to the 3D printed Cu UFG/MC system published by Ramachandramoorthy and Kalacska *et al.* ([18]), we found these results to be in good agreement with both the AD/HT yielding, meaning that the multi-layered thin film proposed here is a fitting model material to further elaborate on the anomalous behavior of the polycrystalline Cu strain rate sensitivity.

In Fig. 3, two anomalous trends in the SRS can be observed: the first one being the saturation of σ_y values of the AD samples at HSR in case of the smaller pillars. This behavior was already reported in Ref. [18], where circular Cu polycrystalline pillars with 2 μm gauge diameters were tested. There it was found that only the pillars with UFG structure exhibited such anomaly, modifying the SRS factor from $m_{\text{UFG}}^{\text{LSR}} = 0.06$ to $m_{\text{UFG}}^{\text{HSR}} = 0.003$. Here, we detected similar behavior, but remarkably, only in the smaller (2.9 μm side length) pillars, leading to the conclusion that the pillar microstructure is not the only driving factor in the anomalous SRS behavior, but also the size of the sample has an additional influence too. In our AD thin films, the SRS factors were found to be close to the already reported values ($m_{\text{AD}}^{\text{LSR}} = 0.03$, $m_{\text{AD}}^{\text{HSR}} = 0.01$). When pillars were fabricated with bigger (4 μm) side length, this anomalous behavior disappeared, and a single m value could describe the SRS within the whole investigated $\dot{\epsilon}$ regime.

The apparent activation volume at the yield point is calculated by the following equation [29, 30]:

$$\Omega = \sqrt{3}k_{\text{B}}T \frac{\partial(\ln \dot{\epsilon})}{\partial(\ln \sigma_y)}, \quad (2)$$

where k_{B} and T are the Boltzmann constant and the temperature, respectively. By using $b = 2.56\text{\AA}$ as the Burgers vector of a $\{111\}\langle 110 \rangle$ dislocation in copper, the calculated activation volumes are $\Omega_{\text{AD}}^{\text{big}} \sim 7.5b^3$, $\Omega_{\text{HT}}^{\text{LSR}} \sim 5.5b^3$ and $\Omega_{\text{AD}}^{\text{small-HSR}} \sim 13b^3$. This suggests that in the LSR regime, the deformation is controlled by the movement of dislocations ($1b^3 - 10b^3$) nucleated at high angle grain boundaries and at surface sources. In the small AD pillars, the increase in Ω suggests a collective dislocation dynamic process ($10b^3 - 100b^3$) [31], meaning that dislocations are created at multiple sources in large numbers upon impact, but their movement is restrained.

The second anomaly in Fig. 3 was discovered upon testing the pillars above 100/s, where the σ_y values unexpectedly increase in the HT samples, regardless of their

size. At LSRs, HT pillars exhibited similar SRS ($m_{\text{HT}}^{\text{LSR}} = 0.02$) as the AD samples. This value matches the m factor reported in Ref. [18] for the MC structured pillars, where a monotonous SRS was also observed in this $\dot{\epsilon}$ regime. However, upon testing the HT pillars at $\dot{\epsilon} = 1000/\text{s}$, the detected m value has increased significantly ($m_{\text{HT}}^{\text{big-HSR}} = 0.19$, $m_{\text{HT}}^{\text{small-HSR}} = 0.11$), showing that at HSR, a transition in the dislocation dynamics happen, resulting in a strain rate hardening regime. This crossover has already been proposed by simulations [32] and demonstrated by large scale impact testing [33], but, to our knowledge, it is the first time to be presented at such small scale, during micromechanical testing. According to Ref. [33], at LSRs, dislocations are thermally activated, while when $\dot{\epsilon}$ exceeds $10^2/\text{s}$, dislocation velocities become so high that the phonon-drag (thermal elastic vibrations) on their motion can no longer be neglected [34], making dislocations much more difficult to move, due to which we observe such an outstanding increase in the σ_y values. Just like in case of the first anomaly, the microstructure plays a crucial part in the SRS, as this deviation will most likely present itself in the AD samples too, only at somewhat higher SRs than what is currently reachable by small scale experiments [35].

4.1. Microstructure evolution

As it can be seen in Fig. 4, and Suppl. Figs. S5 and S7, the heat treatment has increased the initial grain size, that has caused the previously flat Al_2O_3 layers to become rippled, following the curvature of the grains growing in their vicinity. This process can also affect the thickness of the Al_2O_3 layer, too, as the increased grain surface can thin down the interlayer, just like the material of a balloon upon its inflation. One of the striking things to notice was that the grain growth has seemingly reached a final state and further grain growth was blocked even at longer ageing (72 hours was the longest achieved). Even after repeated attempts (initially at 600°C , then 700°C and finally 800°C treatment using different testpieces), the grain growth process was halted. In this system, the Cu grain boundaries could not disappear due to an unknown phenomena. As a possible explanation, the diffusion of the Al (or Al_2O_3) has been proposed, by either *i*) precipitation along grain boundaries, or *ii*) atomic diffusion, as in an intra- or inter-granular manner. High resolution TEM imaging has confirmed the first hypothesis, showing that Al_2O_3 precipitates are located between large grains (marked by white arrows in Fig. 4c), where the curvature of the oxide layer has significantly increased. In order to confirm the second hypothesis based on atomic level diffusion, further experiments will have to be performed, that is out of the scope of the current work. In summary, the aluminum-oxide layer has successfully served its purpose as a thickness (and grain size) controlling barrier, but if larger grains are needed to be designed in the future, the composition or the thickness of the interlayer will need to be modified in the currently investigated system.

| Dataset | Before def. | After def. [m^{-2}] | |
|---------|-------------------------------|--------------------------------|----------------------|
| | (Surface) [m^{-2}] | (Surface) | (Middle) |
| P02 | 1.2×10^{14} | 8.0×10^{14} | 5.4×10^{14} |
| P03 | 1.0×10^{14} | 1.1×10^{15} | – |
| P04 | 1.7×10^{14} | 1.3×10^{15} | 1.1×10^{15} |
| Average | 1.3×10^{14} | – | – |

Table 1: Average ρ_{GND} values based on the HR-EBSD results in Fig. 5.

Furthermore, the decrease of the initial total dislocation density (ρ_{Total}) is also anticipated as a result of high temperature processing. Consequently, hardening rates during deformation could be different for the AD and HT samples. However, it is difficult to separate the effect of ρ_{Total} difference from the influence of the grain boundaries (that also act as dislocation sources) on the yielding and hardening behaviors, therefore this aspect is not discussed further. On the other hand, the resulting dislocation densities from low and high strain rate compressive testing can be investigated in case of the HT samples, where grains are large enough to perform meaningful GND density analysis by HR-EBSD. As the average GND densities shown in Fig. 5 and in Table 1, the initial $\overline{\rho_{\text{GND}}} = 1.3 \times 10^{14} \text{ m}^{-2}$ substantially increases due to external loading. When we compare similar maximum strains at two different SRs ($\varepsilon \sim 18\%$, $\dot{\varepsilon} \in 0.01/\text{s}, 1000/\text{s}$), the resulting ρ_{GND} values are approximately 10 times higher at the surface. By performing *post mortem* FIB cross sectioning, we confirmed that in the middle of these pillars ($\sim 1.6 \mu\text{m}$ below the surface), the average ρ_{GND} values are somewhat lower, that could be attributed to the “surface effect”, allowing facilitated dislocation nucleation (mainly due to the proximity of free surface and FIB damage) close to the facets of the pillars. This is in good agreement with previous GND density measurements on Cu micropillars [36], but it should be noted that during pillar compression, only a fraction of the generated dislocations is geometrically necessary. Additionally, material extrusion happens at the edges without further material constraints, therefore more lattice rotation and more GND generation can occur.

4.2. Strain rate related microstructure transformation

In Ref. [18], when UFG pillars were compressed at HSR, some pillars exhibited grain coarsening in the gauge section, that was attributed to static recrystallization due to the extremely high dislocation densities, and not resulting from dynamical processes during the compression itself [37, 38]. In order to verify the appearance of recrystallization in this thin film (that could potentially modify the deposited coating’s properties after impact), the deformed pillars were mapped by EBSD immediately (~ 2 hours) after micromechanical testing (Suppl. Figs. S5- S7), and after ageing the samples under ambient conditions for 1.5 years (Fig. S8). We found no evidence of abnormal grain growth in these pillars, regardless of the applied SR. The

absence of recrystallization possibly originates from the applied Al_2O_3 interlayers, that conclusively not only exhibit excellent high temperature stability, but could potentially deactivate unwanted microstructure transformation, if the coating is to be operating under extreme conditions.

5. Conclusions

In summary, the created $\text{Cu}/\text{Al}_2\text{O}_3$ multi-layered thin film was successfully tested in its “As Deposited” and “Heat Treated” form, that allowed us to create a model material system to study strain rate sensitivity as a function of the micropillar size and microstructure. The 10 nm thin Al_2O_3 interlayers showed excellent thermal stability, even when long heat treatment was applied. Due to the high temperature processing, Cu grain growth has reached a stabilized state with a microcrystalline structure, grown from the deposited ultrafine-grained formation. After thermal processing, only limited and localized dewetting was observable (while no delamination has occurred) that had, therefore, no influence on the micromechanical characterization, as the coating remained in good mechanical contact with the Si substrate.

During the mechanical data analysis, two anomalous phenomena was identified in the strain rate sensitivity behavior, namely *i*) yield stress saturation in the AD samples when the pillar diameters were below a given threshold, and *ii*) increased strain rate hardening in the HT samples at very high ($\dot{\varepsilon} = 1000/\text{s}$) strain rates. This behavior clearly demonstrates that dislocation nucleation and motion is strongly deformation rate dependent in Cu at high strain rates.

Analysing the *post mortem* surfaces of the deformed pillars it was concluded that the Al_2O_3 interlayers have successfully prevented shear localization (even in the HT pillars), resulting in smooth stress-strain curves and homogeneous deformation throughout the height of the pillars, that produced shape changes in a barrelling manner.

All these conclusions were made on FIB-milled pillars, bearing in mind that the Ga^+ implantation has likely impacted the resulting yield stresses. However, the proposition of such a coating to be considered as a model material to investigate the mechanical behavior of other complex (i.e. 3D printed) materials can finally be accepted by performing a large number of tests in identical conditions, and finding a good correlation between the previously reported yielding behavior and the current work.

GND densities were also studied in detail before and after compression, leading to the observation of slightly higher dislocation densities in the vicinity of the pillars’ edges, resulting in an inhomogeneous distribution within the samples. This most likely plays a key role in the mechanical behavior and results in a transition of the strain rate sensitivity from monotonous to anomalous, when the sample sizes are reduced below a characteristic (microstructure dependent) length scale.

Finally, no recrystallization occurred in the deformed samples, regardless of their size, microstructure or ageing time, that leads to the deduction that the employed Al₂O₃ interlayers successfully prohibit such transformation even when the samples were subjected to high strain rates. This means that the proposed Cu/Al₂O₃ multi-layered system can be applied as a coating to withstand extreme conditions.

Acknowledgement

Matthieu Lenci (Ecole des Mines, St. Etienne) is acknowledged for the TEM imaging.

CRedit statements

S. Kalácska: Conceptualization, Methodology, Validation, Formal analysis, Investigation, Resources, Data Curation, Supervision, Project administration, Writing – Original Draft, Writing – Review & Editing, **L. Pethő:** Investigation, Resources, Writing – Review & Editing, **G. Kermouche:** Resources, Writing – Original Draft, Writing – Review & Editing, **J. Michler:** Resources, Writing – Review & Editing, **P. D. Ispánovity:** Conceptualization, Writing – Original Draft, Writing – Review & Editing

Funding sources

SK and GK were funded by the French National Research Agency (ANR) under the project No. ANR-22-CE08-0012-01 (*INSTINCT*) and No. ANR-20-CE08-0022 (*RATES*). PDI acknowledges the support by the National Research, Development and Innovation Fund of Hungary under project No. NKFIH-FK-138975.

Data Availability

Experimental data generated in this study have been deposited in the Zenodo database at www.doi.org/10.5281/zenodo.12782449.

References

- [1] Z. Wu, X. Chen, Y. Zhang, C. Dun, D. L. Carroll, Z. Hu, In situ electrical properties' investigation and nanofabrication of Ag/Sb₂Te₃ assembled multilayers' film, *Advanced Materials Interfaces* 5 (4) (2017) 1701210. doi:10.1002/admi.201701210.
- [2] J. F. Gómez-Cortés, M. L. Nó, A. Chuvilin, I. Ruiz-Larrea, J. M. S. Juan, Thermal stability of Cu-Al-Ni shape memory alloy thin films obtained by nanometer multilayer deposition, *Nanomaterials* 13 (18) (2023) 2365. doi:10.3390/nano13182605.
- [3] T. Wang, H. P. Ma, J. G. Yang, J. T. Zhu, H. Zhang, J. Feng, S. J. Ding, H. L. Lu, D. W. Zhang, Investigation of the optical and electrical properties of ZnO/Cu/ZnO multilayers grown by atomic layer deposition, *J. Alloys Comp.* 744 (2018) 381–385. doi:10.1016/j.jallcom.2018.02.115.
- [4] B. Yu, P. Woo, U. Erb, Corrosion behaviour of nanocrystalline copper foil in sodium hydroxide solution, *Scripta Materialia* 56 (5) (2007) 1353–356. doi:10.1016/j.scriptamat.2006.11.007.
- [5] B. Giroire, M. A. Ahmad, G. Aubert, L. Teulé-Gay, D. Michau, J. J. Watkins, C. Aymonier, A. Poulon-Quintin, A comparative study of copper thin films deposited using magnetron sputtering and supercritical fluid deposition techniques, *Thin Solid Films* 643 (2017) 53–59. doi:10.1016/j.tsf.2017.09.002.
- [6] K. Mech, L. Kowalik, R. Zabinski, Cu thin films deposited by dc magnetron sputtering for contact surfaces on electronic components, *Archives of Metallurgy and Materials* 56 (4) (2011) 903–908. doi:10.2478/v10172-011-0099-4.
- [7] T. Xie, T. E. J. Edwards, N. M. della Ventura, D. Casari, E. Huszár, L. Fu, L. Zhou, X. Maeder, J. J. Schwiedrzik, I. Utke, J. Michler, L. Pethő, Synthesis of model al-al₂o₃ multilayer systems with monolayer oxide thickness control by circumventing native oxidation, *Thin Solid Films* 711 (2020) 138287. doi:10.1016/j.tsf.2020.138287.
- [8] T. E. J. Edwards, T. Xie, N. M. della Ventura, D. Casari, C. Guerra, E. Huszár, X. Maeder, J. J. Schwiedrzik, I. Utke, L. Pethő, J. Michler, On the thinnest al₂o₃ interlayers in al-based nanolaminates to enhance strength, and the role of constraint, *Acta Materialia* 240 (2022) 118345. doi:10.1016/j.actamat.2022.118345.
- [9] N. Rohbeck, R. Ramachandramoorthy, D. Casari, P. Schürch, T. E. J. Edwards, L. Schilinsky, L. Philippe, J. Schwiedrzik, J. Michler, Effect of high strain rates and temperature on the micromechanical properties of 3D-printed polymer structures made by two-photon lithography, *Materials & Design* 195 (2020) 108977. doi:10.1016/j.matdes.2020.108977.
- [10] R. Ramachandramoorthy, F. Yang, D. Casari, M. Stolpe, M. Jain, J. Schwiedrzik, J. Michler, J. J. Kruzic, J. P. Best, High strain rate in situ micropillar compression of a Zr-based metallic glass, *J. Mat. Res.* 36 (2021) 2325–2336. doi:10.1557/s43578-021-00187-5.
- [11] N. M. della Ventura, A. Sharma, M. Jain, S. Kalácska, T. E. J. Edwards, C. Cayron, R. Logé, J. Michler, X. Maeder, Evolution of deformation twinning mechanisms in magnesium from low to high strain rates, *Materials & Design* (2022) 110646doi:10.1016/j.matdes.2022.110646.
- [12] J. Schwiedrzik, R. Ramachandramoorthy, T. E. J. Edwards, P. Schürch, D. Casari, M. J. Duarte, G. Mohanty, G. Dehm, X. Maeder, L. Philippe, J. M. Breguet, J. Michler, Dynamic cryo-mechanical properties of additively manufactured nanocrystalline nickel 3D microarchitectures, *Materials & Design* 220 (2022) 110836. doi:10.1016/j.matdes.2022.110836.
- [13] N. M. della Ventura, A. Sharma, C. Cayron, S. Kalácska, T. E. J. Edwards, C. Peruzzi, M. Jain, J. T. Pürstl, R. E. Logé, J. Michler, X. Maeder, Response of magnesium microcrystals to c-axis compression and contraction loadings at low and high strain rates, *Acta Materialia* 248 (2023) 118762. doi:10.1016/j.actamat.2023.118762.
- [14] S. Cheng, E. Ma, Y. Wang, L. Kecskes, K. Youssef, C. Koch, U. Trociewitz, K. Han, Tensile properties of in situ consolidated nanocrystalline Cu, *Acta Materialia* 53 (5) (2005) 1521–1533. doi:10.1016/j.actamat.2004.12.005.
- [15] Soni, M. J. Shekh, S. Sharma, S. Mishra, Strain rate sensitivity behaviour of the thin films of Al, Al-Si and nanocomposite Al-Si-N: A comparative study, *Materials Characterization* 169 (2020) 110589. doi:10.1016/j.matchar.2020.110589.
- [16] R. B. Figueiredo, W. Wolf, T. G. Langdon, Effect of grain size on strength and strain rate sensitivity in the CrMnFeCoNi high-entropy alloy, *J. Mat. Res. Techn.* 20 (2022) 2358–2368. doi:10.1016/j.jmrt.2022.07.181.
- [17] J. Zhang, X. Liang, P. Zhang, K. Wu, G. Liu, J. Sun, Emergence of external size effects in the bulk-scale polycrystal to small-scale single-crystal transition: A maximum in the strength and strain-rate sensitivity of multicrystalline Cu micropillars, *Acta Materialia* 66 (2014) 302–316. doi:10.1016/j.actamat.2013.11.018.

- [18] R. Ramachandramoorthy, S. Kalácska, G. Poras, J. Schwiedrzik, T. E. J. Edwards, X. Maeder, T. Merle, G. Ercolano, W. Koelmans, J. Michler, Anomalous high strain rate compressive behavior of additively manufactured copper micropillars, *Applied Materials Today* 27 (2022) 101415. doi:10.1016/j.apmt.2022.101415.
- [19] A. J. Wilkinson, G. Meaden, D. J. Dingley, High-resolution elastic strain measurement from electron backscatter diffraction patterns: new levels of sensitivity, *Ultramicroscopy* 106 (4-5) (2006) 307–313. doi:10.1016/j.ultramicro.2005.10.001.
- [20] S. Kalácska, J. Ast, P. D. Ispánovity, J. Michler, X. Maeder, 3D HR-EBSD characterization of the plastic zone around crack tips in tungsten single crystals at the micron scale, *Acta Materialia* 200 (2020) 211–222. doi:10.1016/j.actamat.2020.09.009.
- [21] Y. Xiao, J. Wehrs, H. Ma, T. Al-Samman, S. Korte-Kerzel, M. Göken, J. Michler, R. Spolenak, J. Wheeler, Investigation of the deformation behavior of aluminum micropillars produced by focused ion beam machining using Ga and Xe ions, *Thin Solid Films* 127 (2017) 191–194. doi:10.1016/j.scriptamat.2016.08.028.
- [22] Y. Xiao, V. Maier-Kiener, J. Michler, R. Spolenak, J. Wheeler, Deformation behavior of aluminum pillars produced by Xe and Ga focused ion beams: Insights from strain rate jump tests, *Materials & Design* 181 (2019) 107914. doi:10.1016/j.matdes.2019.107914.
- [23] S. Breumier, S. Sao-Joao, A. Villani, M. Lévesque, G. Kermouche, High strain rate micro-compression for crystal plasticity constitutive law parameters identification, *Materials & Design* 193 (2020) 108789. doi:10.1016/j.matdes.2020.108789.
- [24] J. Schiotz, K. W. Jacobsen, A maximum in the strength of nanocrystalline copper, *Science* 301 (5638) (2003) 1357–1359. doi:10.1126/science.1086636.
- [25] R. K. Guduru, K. L. Murty, K. M. Youssef, R. O. Scattergood, C. C. Koch, Mechanical behavior of nanocrystalline copper, *Mat. Sci. Eng. A* 463 (5638) (2007) 1357–1359. doi:10.1016/j.msea.2006.07.165.
- [26] W. Smith, J. Hashemi, *Foundations of Materials Science and Engineering*, McGraw-Hill series in materials science and engineering, McGraw-Hill, 2006.
URL <https://books.google.fr/books?id=1QUESgAACAAJ>
- [27] L. Sun, X. He, J. Lu, Nanotwinned and hierarchical nanotwinned metals: a review of experimental, computational and theoretical efforts, *npj Computational Materials* 4 (2018) 6. doi:10.1038/s41524-018-0062-2.
- [28] A. A. Tiarniyu, E. L. Pang, X. Chen, J. M. LeBeau, K. A. Nelson, C. A. Schuh, Nanotwinning-assisted dynamic recrystallization at high strains and strain rates, *Nature Materials* 21 (2022) 786–794. doi:10.1038/s41563-022-01250-0.
- [29] G. Schoeck, The activation energy of dislocation movement, *Physica Status Solidi B* 8 (2) (1965) 499–507. doi:10.1002/pssb.19650080209.
- [30] A. Krausz, A deformation kinetics analysis of the stress sensitivity, *Materials Science and Engineering* 26 (1) (1976) 65–71. doi:10.1016/0025-5416(76)90226-3.
- [31] A. T. Jennings, J. Li, J. R. Greer, Emergence of strain-rate sensitivity in cu nanopillars: transition from dislocation multiplication to dislocation nucleation, *Acta Materialia* 59 (14) (2011) 5627–5637. doi:10.1016/j.actamat.2011.05.038.
- [32] H. Fan, Q. Wang, J. A. El-Awady, D. Raabe, M. Zaiser, Strain rate dependency of dislocation plasticity, *Nature Communication* 12 (2021) 1845. doi:10.1038/s41467-021-21939-1.
- [33] N. Kumar, Q. Ying, X. Nie, R. Mishra, Z. Tang, P. Liaw, R. Brennan, K. Doherty, K. Cho, High strain-rate compressive deformation behavior of the Al_{0.1}CrFeCoNi high entropy alloy, *Materials & Design* 86 (2015) 598–602. doi:10.1016/j.matdes.2015.07.161.
- [34] M. Meyers, *Dynamic Behavior of Materials*, J. Wiley and Sons, 1994.
- [35] Z. N. Mao, X. H. An, X. Z. Liao, J. T. Wang, Opposite grain size dependence of strain rate sensitivity of copper at low vs high strain rates, *Mat. Sci. Eng. A* 738 (4) (2018) 430–438. doi:10.1016/j.msea.2018.09.018.
- [36] S. Kalácska, Z. Dankházi, G. Zilahi, X. Maeder, J. Michler, P. D. Ispánovity, I. Groma, Investigation of geometrically necessary dislocation structures in compressed cu micropillars by 3-dimensional hr-ebbsd, *Mat. Sci. Eng. A* 770 (2020) 138499. doi:10.1016/j.msea.2019.138499.
- [37] U. Andrade, M. Meyers, K. Vecchio, A. Chokshi, Dynamic recrystallization in high-strain, high-strain-rate plastic deformation of copper, *Acta Metall. Mater.* 42 (9) (1994) 3183–3195. doi:10.1016/0956-7151(94)90417-0.
- [38] R. Thevamaran, O. Lawal, S. Yazdi, S. J. Jeon, J. H. Lee, E. L. Thomas, Dynamic creation and evolution of gradient nanostructure in single-crystal metallic microcubes, *Science* 354 (6310) (2022) 312–316. doi:10.1126/science.aag17.

Supplementary Materials for Anomalous strain rate sensitivity of a Cu/Al₂O₃ multi-layered thin film

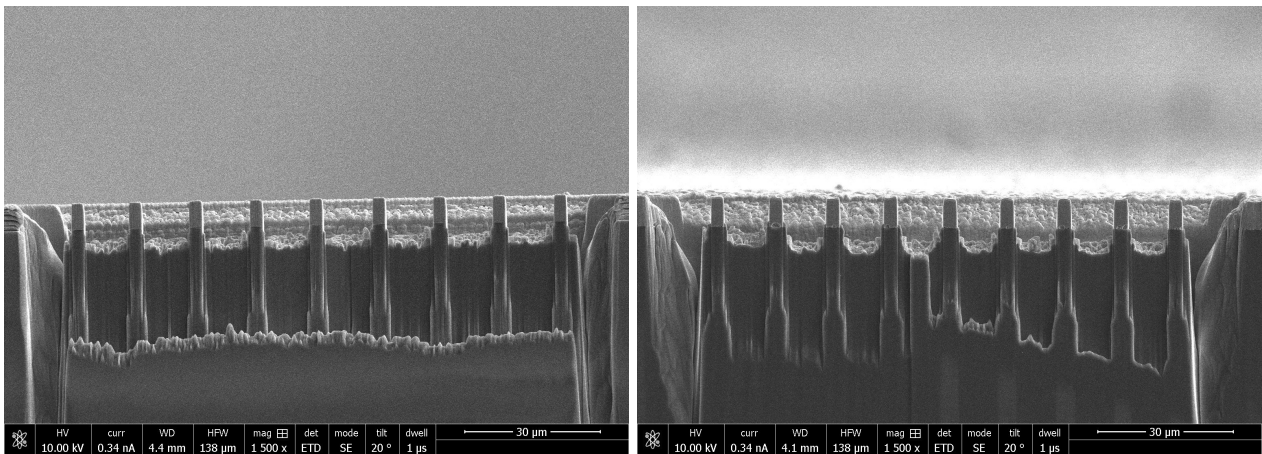
Szilvia Kalácska^{a,b,*}, László Pethő^b, Guillaume Kermouche^a, Johann Michler^b, Péter D. Ispánovity^c

^a Mines Saint-Etienne, Univ Lyon, CNRS, UMR 5307 LGF, Centre SMS, 158 cours Fauriel 42023 Saint-Étienne, France

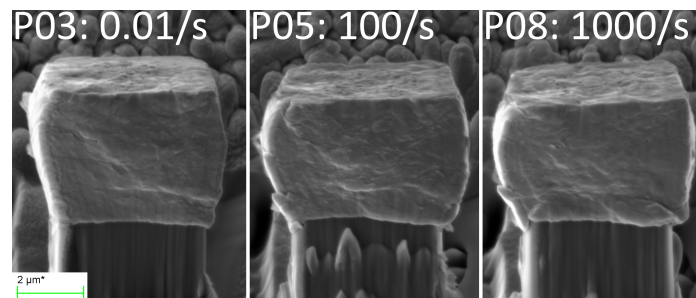
^b Empa, Swiss Federal Laboratories for Materials Science and Technology, Laboratory of Mechanics of Materials and Nanostructures, CH-3602 Thun, Feuerwerkerstrasse 39. Switzerland

^c Eötvös Loránd University, Pázmány P. stny 1/a, 1117 Budapest, Hungary

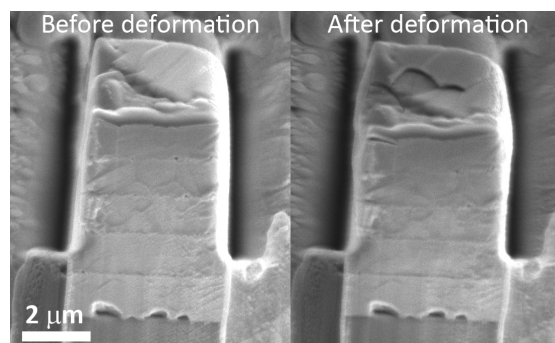
Data repository available at: www.doi.org/10.5281/zenodo.12782449



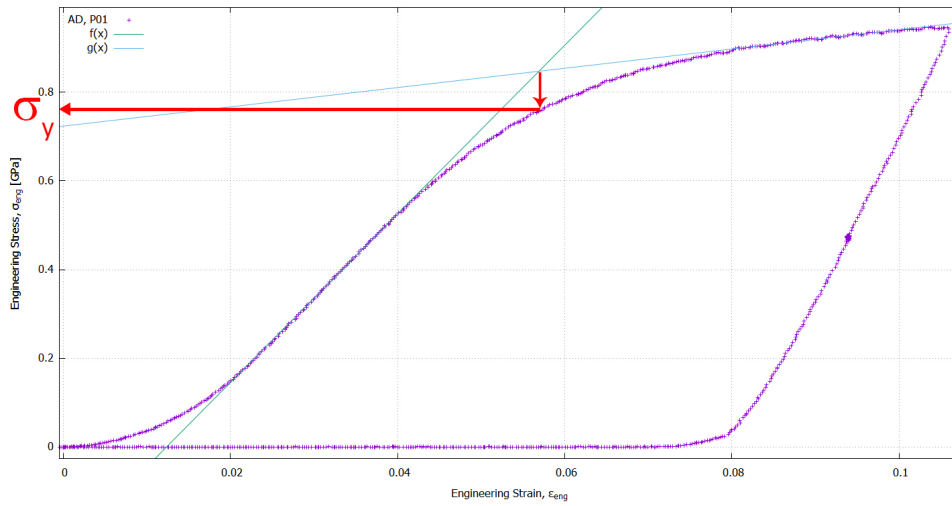
Suppl. Figure S 1: **overview**, 2.9 μm (small) pillars: (left) As Deposited, (right) Heat Treated.



Suppl. Figure S 2: **As Deposited** pillars after deformation.

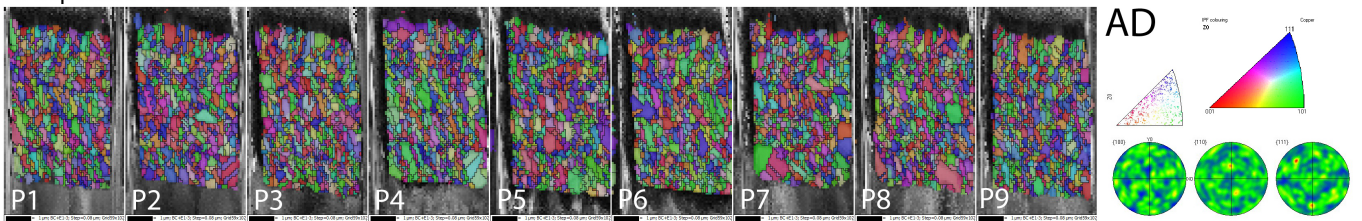


Suppl. Figure S 3: **Heat Treated** pillar P03, before and after deformation.

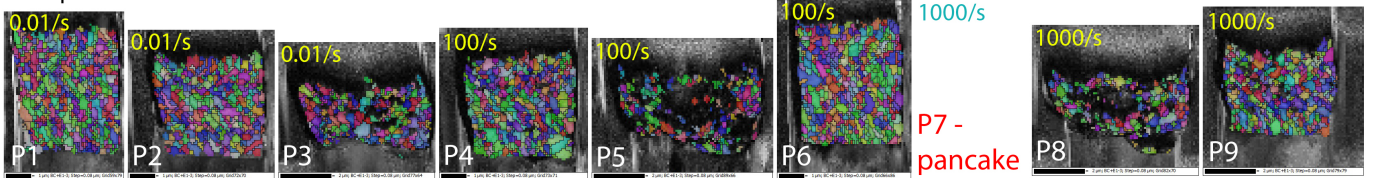


Suppl. Figure S 4: **Yield stress determination procedure**, pillar "AD" P01. This method was used to be consistent even at high strain rates, where the "ringing effect" introduces oscillations to the stress-strain curve.

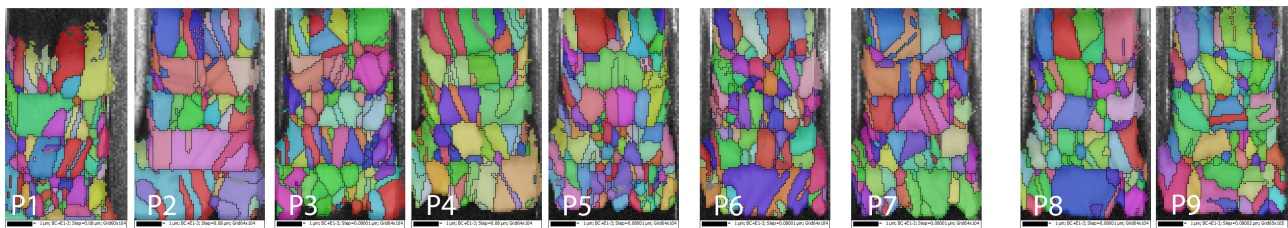
As deposited - before deformation



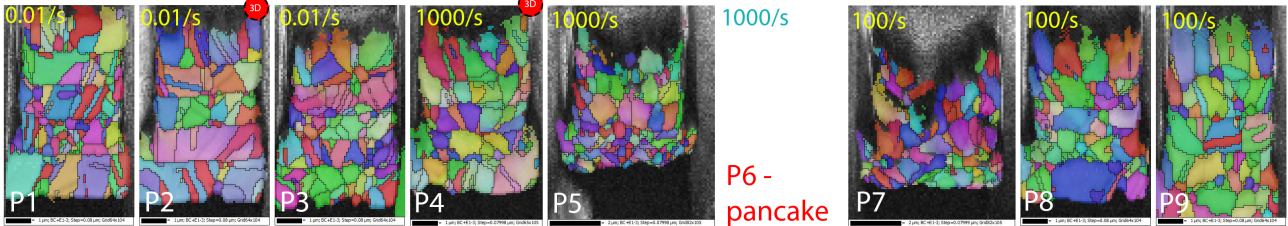
As deposited - after deformation



Heat treated - before deformation

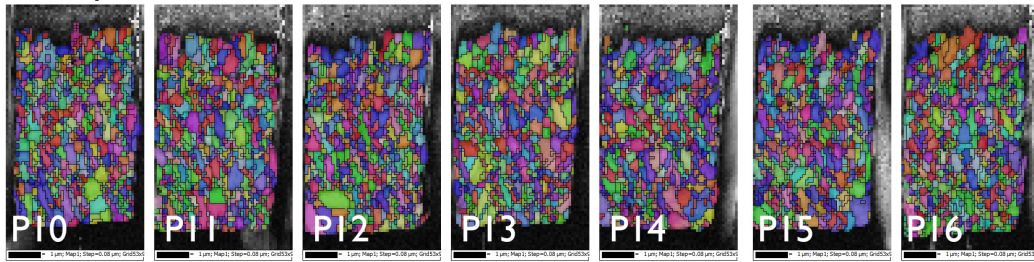


Heat treated - after deformation

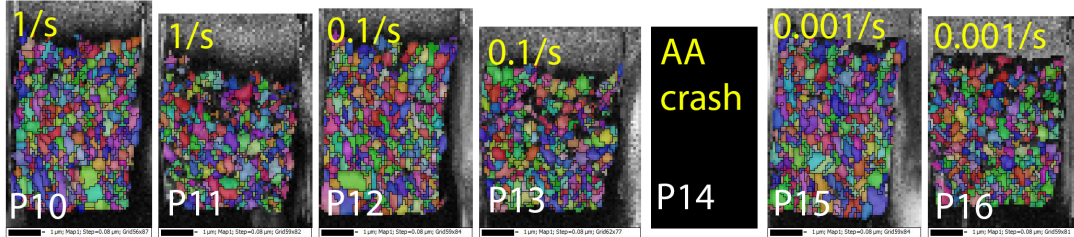


Suppl. Figure S 5: **EBSD results**, 4 μm (big) pillars. Z directional inverse pole figure (IPF Z) colouring is shown together with band contract (BC, greyscale) imaging, before and after deformation. In the to right corner the full IPF triangle is shown along with the registered grain colours plotted inside the IPF triangle for the as deposited (AD) case. Pole figures plotted for the X, Y and D directions show no specific texture in the AD sample. Red dots on the EBSD maps highlight the two pillars that were analysed by *post mortem* 3D HR-EBSD.

As deposited - before deformation

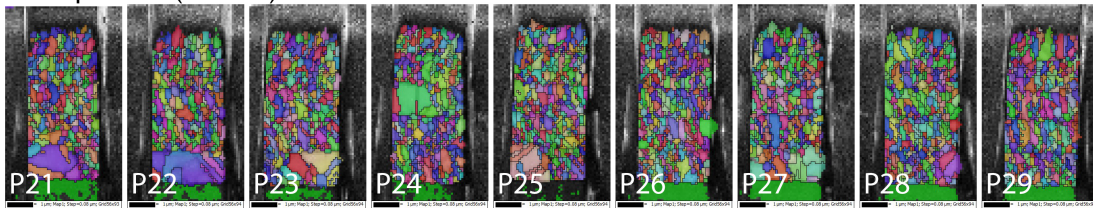


As deposited - after deformation

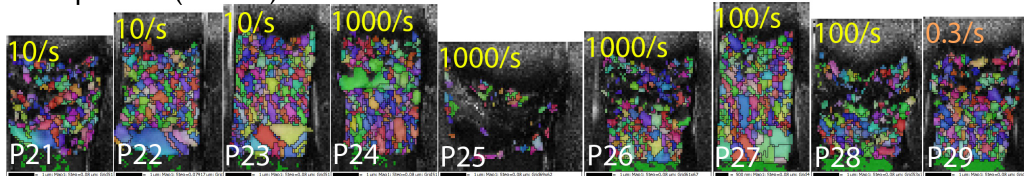


Suppl. Figure S 6: **EBSD results**, 4.0 μm pillars, 2nd batch (for more statistics). Z directional inverse pole figure (IPF Z) colouring is shown together with band contract (BC, greyscale) imaging, before and after deformation. "AA crash" refers to the accidental touch of the pillar upon auto approach procedure, which resulted in an unknown deformation state, therefore this pillar was excluded from the analysis.

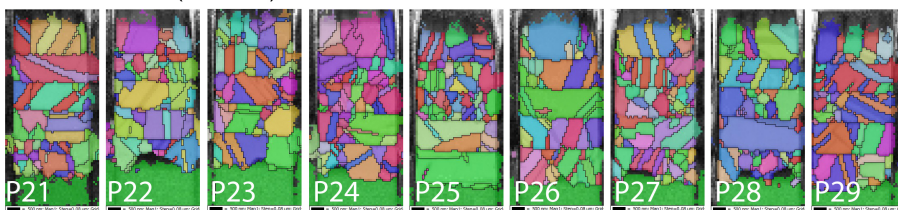
As deposited (SMALL) - before deformation



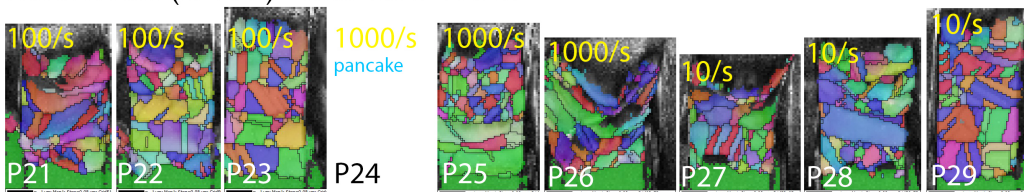
As deposited (SMALL) - after deformation



Heat treated (SMALL) - before deformation

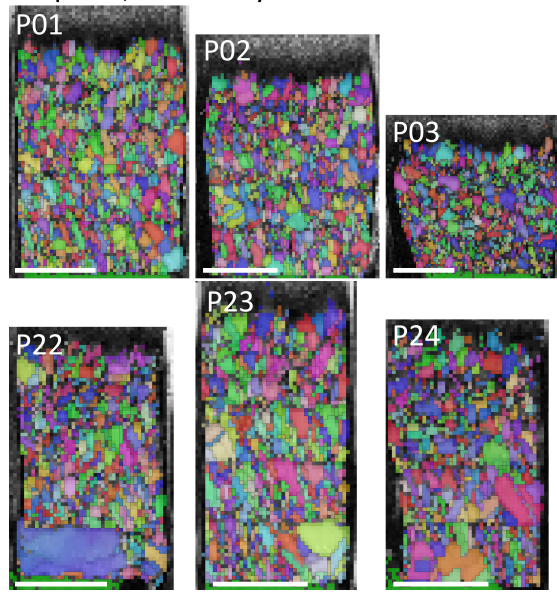


Heat treated (SMALL) - after deformation

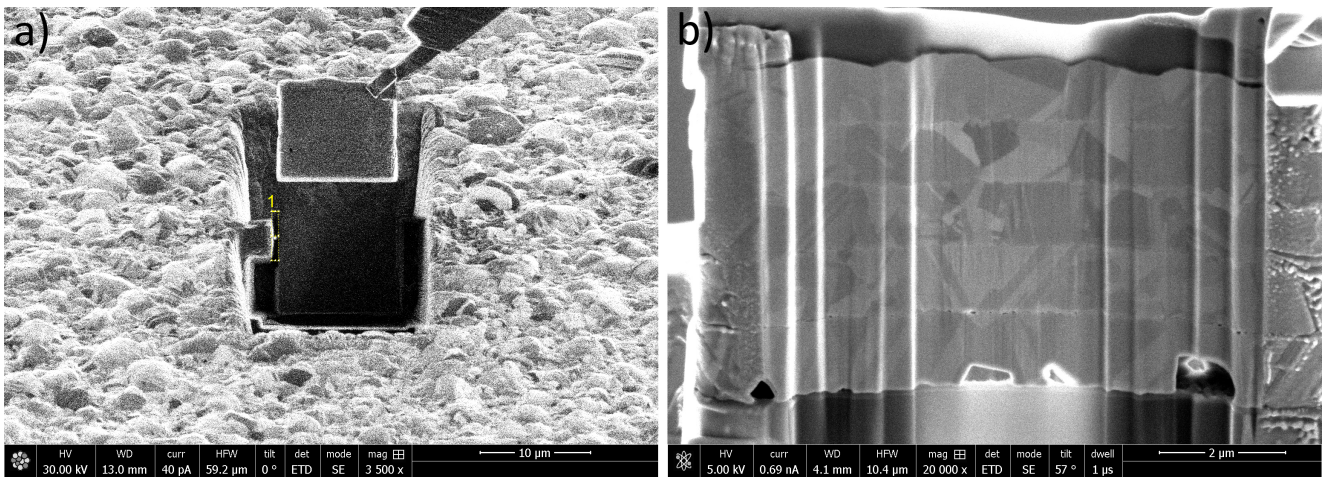


Suppl. Figure S 7: **EBSD results**, 2.9 μm pillars (for size effect). Z directional inverse pole figure (IPF Z) colouring is shown together with band contract (BC, greyscale) imaging, before and after deformation.

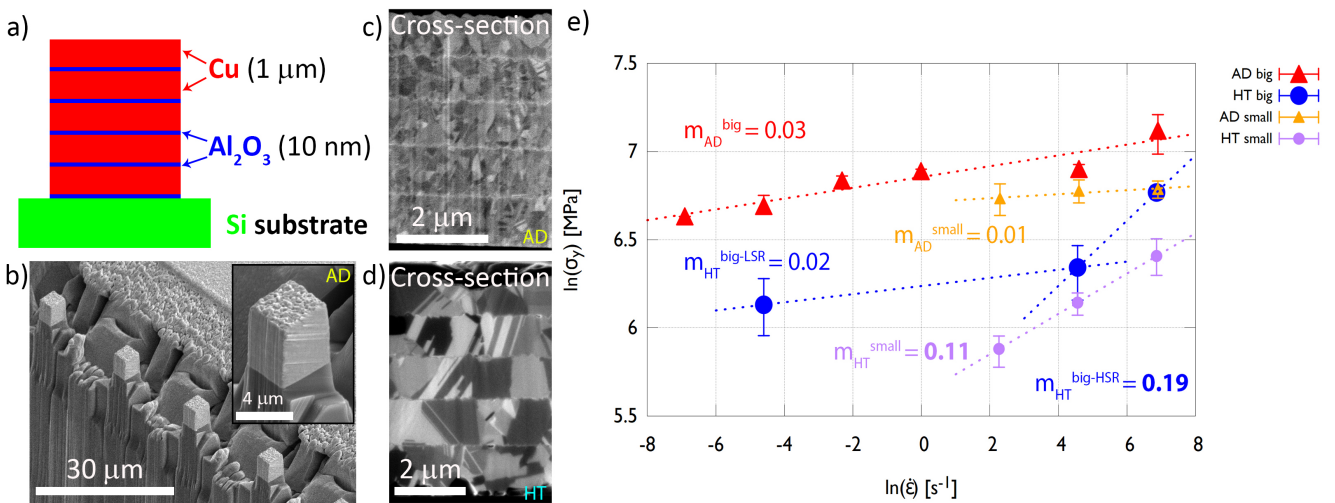
AD pillars, after 1.5 years



Suppl. Figure S 8: EBSD results of the deformed AD pillars, aged for 1.5 years, repolished by FIB.



Suppl. Figure S 9: TEM lamella preparation. a) snapshot during the liftout process, b) image taken during the thinning.



Suppl. Figure S 10: Graphical Abstract